ACS APPLIED MATERIALS & INTERFACES

www.acsami.org

Research Article

Decoupling Individual Optical Nanosensor Responses Using a Spin-Coated Hydrogel Platform

Matthew Card, Raisa Alejandro, and Daniel Roxbury*

Cite This: *ACS Appl. Mater. Interfaces* 2023, 15, 1772−1783

Read Online

ACCESS | Metrics & More | Article Recommendations | Supporting Information

ABSTRACT: Significant advances have been made in fields such as nanotechnology and biomedicine using the unique properties of single-walled carbon nanotubes (SWCNTs). Specifically, SWCNTs are used as near-infrared fluorescence sensors in the solution phase to detect a wide array of biologically relevant analytes. However, solution-based sensing has several limitations, including limited sensitivity and poor spatial resolution. We have therefore devised a new spin-coated poly(ethylene glycol) diacrylate (PEG-DA) hydrogel platform to examine individual DNA-functionalized SWCNTs (DNA-SWCNTs) in their native aqueous state and have subsequently used this platform to investigate the temporal modulations of each SWCNT in response to a model analyte. A strong surfactant, sodium deoxycholate (SDC), was chosen as the model analyte as it rapidly exchanges with DNA oligonucleotides on the SWCNT surface, modulating several optical properties of the SWCNTs and demonstrating multiparameter analyte detection. Upon addition of SDC, we observed time-dependent spectral modulations in the emission center wavelengths and peak intensities of the individual SWCNTs, indicative of a DNA-to-surfactant exchange process. Interestingly, we found that the modulations in the peak intensities, as determined by kinetic data, were significantly delayed when compared to their center wavelength counterparts, suggesting a potential decoupling of the response of these two spectral features. We used a 1-D diffusion model to relate the local SDC concentration to the spectral response of each SWCNT and created dose−response curves. The peak intensity shifts at a higher SDC concentration than the center wavelength, indicating a potential change in the conformation of the surfactant molecules adsorbed to the SWCNT sidewall after the initial exchange process. This platform allows for a unique single-molecule analysis technique that is significantly more sensitive and modifiable than utilizing SWCNTs in the solution phase.

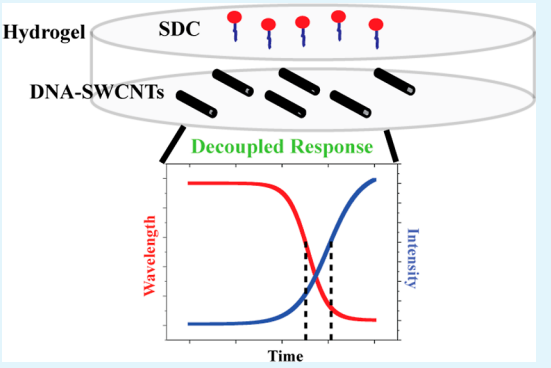

KEYWORDS: *single-molecule detection, optical sensors, hyperspectral imaging, near-infrared fluorescence, hydrogel*

INTRODUCTION

Single-walled carbon nanotubes (SWCNTs) have been used extensively in a variety of applications due to their unique optical,[1] physical,[2] and electrical properties.[3] SWCNTs exist in a family of differing chiral species, denoted by (*n*,*m*), giving rise to distinct exciton binding energies.[4,5] Specifically under visible or near-infrared (NIR) excitation, semiconducting SWCNTs exhibit photostable[6] and sensitive[7] band-gap fluorescence in the NIR region of the spectrum.[8] Although SWCNTs are inherently hydrophobic in their native state, they can be noncovalently functionalized with various amphiphilic molecules to create a stable suspension in an aqueous solution.[9] Therefore, the chemical nature of the resultant SWCNT hybrids is highly tunable[10] and can be made selective to a target analyte by modifying their surface functionalization.[11] These unique properties allow SWCNTs to be used in many biological applications, namely, targeted imaging and sensing.

Single-stranded DNA-functionalized SWCNT hybrids (DNA-SWCNTs) are especially useful in biosensing applications due to their enhanced stability in biological environments[12] and in vivo biocompatibility.[13] Understanding the stability of DNA−SWCNT hybrids is crucial to the development of such biosensors and has been the focus of many recent investigations within our and several other labs.[14−19] The hybrid stability is directly related to the binding energy of the DNA oligonucleotide on the SWCNT surface.[9,12] When surfactant molecules interact with a DNA−SWCNT at a high-enough concentration, they exchange with the DNA oligonucleotides on the SWCNT surface via a higher affinity to adsorb onto the SWCNT sidewall.[20,21] The rate of this exchange can be directly correlated with the DNA binding strength, where a faster exchange indicates a weaker affinity of the DNA to the SWCNT sidewall and therefore lower

Received: September 14, 2022
Accepted: December 12, 2022
Published: December 22, 2022

stability.[15] The concentration required for this is notably lower than the critical micelle concentration, likely due to the high contribution to the hydrophobicity from the bare carbon nanotube surface.[15] In solution, the surfactant exchange generally causes a large blue shift in the emission wavelength of the fluorescence spectra, as well as a large increase in fluorescence intensity via a change in the local dielectric environment.[15] A DNA−SWCNT typically exposes bare areas of the SWCNT surface[22,23] which are in contact with the solvent and thus directly modulates the exciton binding energy.[6,22] When the surfactant replaces the DNA strands, a micelle structure is formed around the SWCNT, preventing the solvent from making contact with the surface.[24] This new, more stable conformation also likely limits conventional mechanisms of the photoluminescence quenching of DNA-SWCNTs, such as pH,[25] ionic strength,[26] and even oxygen adsorption.[27]

In the solution phase, SWCNTs have been used to selectively detect analytes by reporting the variations in fluorescence properties caused by conformational changes of the functionalization near the SWCNT surface.[7] There are however certain limitations in using SWCNTs as NIR sensors in the solution phase. For instance, SWCNTs can often aggregate in solution in response to an analyte via electrostatic interactions, effectively modulating fundamental optical properties such as emission wavelength and integrated intensity, potentially confounding any readout of the sensor.[28,29] Additionally, under microscopic analysis, the determination of SWCNT properties in solution is limited, given that individual SWCNTs cannot easily be resolved over a long period of time due to Brownian motion. Therefore, new strategies are required to enhance the applicability of these types of nanosensors.

With all of their constituent atoms residing on the surface, SWCNTs are highly sensitive to their environment and, thus, single-molecule detection has been reported via optical modulation.[30] Due to their profound sensitivity, SWCNTs have been studied for applications in single-molecule detection recently through their use as field-effect transistors (FETs)[31,32] or fluorescence sensors.[33,34] Single-molecule detection is the absolute lowest limit of detection possible, which importantly avoids averaging data as in ensemble measurements.[35] It allows for a fundamental understanding of analyte interactions and the heterogeneous properties of the analyte and sensor, if applicable.[36] In particular, even single-chirality suspensions of SWCNTs display a large degree of heterogeneity in their physical features, including length,[14] degrees of surface functionalization,[37] and the number of defects.[38] We previously demonstrated the inherent optical heterogeneity present in individual SWCNTs.[39] Therefore, in order to lower the limit of detection in the development of next-generation SWCNT-based biosensors, it is crucial to accurately understand and account for these effects.

Hydrogels are networks of crosslinked polymers that swell in the presence of water.[40] There are many ways to classify hydrogels, for example, charge-based classification, where the hydrogels are cationic, anionic, neutral, or ampholytic.[41] In addition, many hydrogels can be either chemically (covalently) or physically (noncovalently) crosslinked.[42] It has been shown that SWCNTs can be immobilized in a hydrogel in order to retain their optical properties while simultaneously modeling an aqueous solution.[8,43−45] SWCNT−hydrogel systems have been used in a variety of sensing applications, given their unique combination of solution-phase and substrate properties.[44,46] However, standard methods of preparation make it difficult to sensitively probe the diffusion properties of a target analyte, which is important for characterizing analyte−SWCNT interactions. There is thus a need for an easily modifiable platform, for instance, a hydrogel system containing a single layer of nanosensors at a defined distance from the surface. Such a platform would allow for the observation and measurement of modulations in optical properties on the same SWCNTs over extended periods of time, thus enabling various types of kinetics analyses. Additionally, NIR hyperspectral imaging has the advantage of acquiring wavelength, intensity, and full width at half-maximum (fwhm) values rather than standard intensity images from NIR fluorescence microscopy. Furthermore, observing individual SWCNTs in this way has the distinct advantage of being able to be used in both characterization and sensing applications. A given SWCNT response toward a target analyte can be correlated with the concentration of that analyte or to the specific physical properties or surface functionalization of the observed SWCNT.

Here, using NIR hyperspectral fluorescence microscopy, we demonstrate a modifiable hydrogel platform for analysis of the diffusion kinetics of target analytes and their interactions with individual SWCNTs over time. First, DNA-SWCNTs were encapsulated in a spin-coated hydrogel platform at a defined distance from the hydrogel surface. We next observed modulations in emission wavelength and intensity on individual SWCNTs upon the addition of a model analyte, sodium deoxycholate (SDC). SDC slowly diffuses into the hydrogel, rapidly exchanging with the DNA on the SWCNT surface once a critical surfactant concentration is reached, allowing us to obtain pertinent information about DNA−SWCNT hybrids. We demonstrate that our platform can be used for the characterization of properties such as DNA binding strength and dynamic optical response, as well as for sensitive analyte detection. Significant differences were observed in the modulations of wavelength and intensity, suggesting the various spectral features may be controlled by different mechanisms. Lastly, we use a 1-D diffusion model to correlate the diffusion of SDC in our platform to the changes in the optical properties of SWCNTs over time. We then further investigate the differences in SWCNT spectral features and propose mechanisms for the observed differences.

RESULTS AND DISCUSSION

In order to image individual, immobilized SWCNTs, a spin-coated hydrogel platform was fabricated, modified from a previous procedure (Figure 1a).[39] Poly(ethylene glycol) diacrylate (PEG-DA) was chosen as it is a polymer that can be rapidly cured with UV light into a stable hydrogel in the presence of a photoinitiator. It is also used extensively in biomedical applications due to its neutral nature and biocompatibility.[47,48] To create the platform, a small amount of a PEG-DA and photoinitiator, lithium phenyl-2,4,6-trimethylbenzoylphosphinate (LAP), solution was deposited onto a Petri dish containing a glass coverslip. The Petri dish with the PEG-DA precursor solution was then placed onto a spin-coater, where the lid was closed and a small 365 nm UV lamp was positioned over a small opening on the lid. The sample was slowly spun in increments of increasing speed with simultaneous UV illumination in order to carefully leave a thin layer of PEG-DA on the glass surface. This step was crucial as

https://doi.org/10.1021/acsami.2c16596
ACS Appl. Mater. Interfaces 2023, 15, 1772−1783

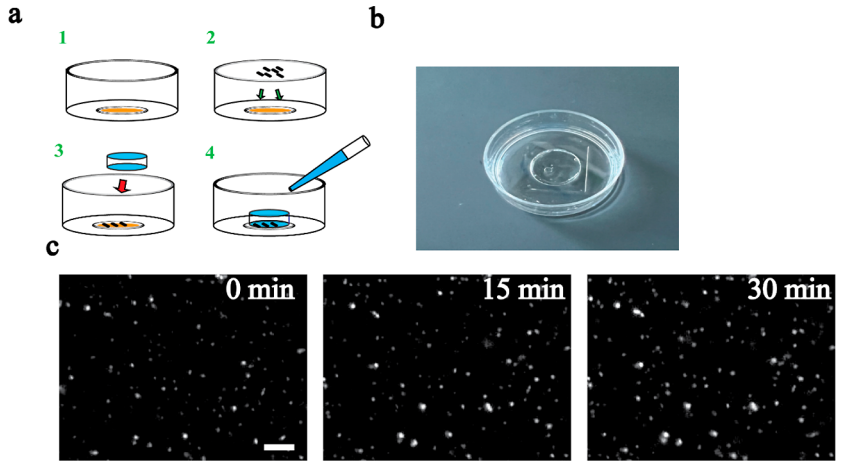

Figure 1. Demonstration of the spin-coated PEG-DA platform with DNA-SWCNTs. (a) Illustration of the fabrication of the PEG-DA platform. This consists of four main steps: (1) spin-coating of the bottom (orange) PEG-DA layer and crosslinking, (2) spin-coating of DNA-SWCNTs, (3) addition of the preformed PEG-DA layer and crosslinking, and finally (4) addition of excess phosphate-buffered saline to fully swell the hydrogel platform. (b) Photograph of the as-prepared PEG-DA platform. (c) Broadband NIR fluorescence images of DNA−SWCNTs in the hydrogel platform in time after the addition of 2% SDC. A global contrast is applied to all of the grayscale images. The scale bar is 5 μm.

the viscosity of the solution must be slowly increased such that it will not be removed via centripetal force. The sample was then left to UV cure for 10 min. After the bottom layer of the hydrogel was fully crosslinked, it was lightly washed with phosphate-buffered saline (PBS) to remove any excess free radicals that were generated by the photoinitiator. A separate layer of the PEG-DA hydrogel was prepared in another glass-bottom Petri dish by placing a coverslip over the hole filled with the precursor solution and then UV-curing in a similar manner. In parallel, a solution of DNA−SWCNTs (see Materials and Methods) was spin-coated onto the bottom hydrogel layer. CoMoCAT SG65i SWCNTs were chosen as they are dominated by the (6,5)-SWCNT,[49] meaning that the final platform will essentially contain SWCNTs of a single chirality. The second layer was then carefully placed on top of the PEG-DA layer with SWCNTs and then crosslinked to the bottom layer again with UV curing, and the excess precursor solution was placed around the seam of the two layers. The final platform creates one-dimensional (1-D) analyte diffusion from the top of the hydrogel to the layer of SWCNTs since the top layer of hydrogel is significantly wider than it is thick. Lastly, the hydrogel was washed three times with PBS, allowed to equilibrate for 10 min between each wash, and then 2 mL of PBS was added to the Petri dish to allow the hydrogel to swell (Figure 1b). It has been demonstrated that free DNA can be removed in both the solution phase[50,51] via filtering and in a hydrogel by washing the sample with aqueous solutions.[52,53] Therefore, a large majority of the free DNA is expected to be removed from the platform after washing the hydrogel three times and additionally with the final addition of PBS.

The resulting hydrogel system was then characterized by finding the swelled thickness, swelling ratio, and mesh size. The thickness of the hydrogel was measured to be 1.3 mm after swelling for 4 h. This value was constant even after 24 h of incubation with PBS. The mesh size was found using a previously described method.[54,55] The swelling ratio (q_F)was first determined as

$$q_F = \frac{m_{wet}}{m_{dry}} \tag{1}$$

where m_{wet} is the mass of the hydrogel in its swelled state and m_{dry} is the mass of the fully dried hydrogel. The following equation can then be used to calculate the volume fraction of the polymer (v_2)

$$v_2 = \frac{1}{1 + (q_F - 1)\rho_p/\rho_w} \tag{2}$$

where $\rho_P$and ρ_W are the density of PEG-DA (1.12 g/cm^3) and water (1 g/cm^3) respectively.

The crosslink density (n) was determined by

$$n = -[\ln(1 - v_2) + v_2 + \chi_1 v_2^2]/[V_1(v_2^{1/3} - 0.5v_2)] \tag{3}$$

where χ_1 is the Flory−Huggins interaction parameter (0.426)[56] and V_1 is the molar volume of water, 18 cm^3. The mesh or pore size of the hydrogel (ξ) can then be approximated by

$$\xi = v_2^{-1/3} l \times \left[\left(\frac{2\rho_p}{n}\right)/M_r\right]^{1/2} C_n^{1/2} \tag{4}$$

where l is the carbon−carbon bond length of the PEG monomer (1.5 Å), M_r is the molecular weight of the repeat unit (44 g/mol), and C_n is the characteristic ratio, which is 4 for PEG-DA.[57] The swelling ratio was experimentally determined to be 10.1 ± 0.52; thus, the mesh size was calculated to be 14 nm, which is close to PEG-DA hydrogels with similar fabrication parameters in the literature.[58] The average size of the examined DNA-SWCNTs (~100 nm)[14] is much higher than the mesh size of 14 nm, so there is expected to be minimal diffusion of SWCNTs throughout the hydrogel platform.

The utility of the platform was then demonstrated by spiking in the model analyte SDC surfactant. The surfactant exchange process can be visualized in Figure S1. Broadband NIR fluorescence images (900−1600 nm) were obtained immediately after the addition of the surfactant and in subsequent 15 min intervals (Figure 1c). By 30 min, the fluorescence intensities of the DNA-SWCNTs within the hydrogel significantly increased as expected, while they remained in the same spatial position. Given that the SWCNTs in the hydrogel platform are trapped between two hydrogel layers,

https://doi.org/10.1021/acsami.2c16596
ACS Appl. Mater. Interfaces 2023, 15, 1772−1783

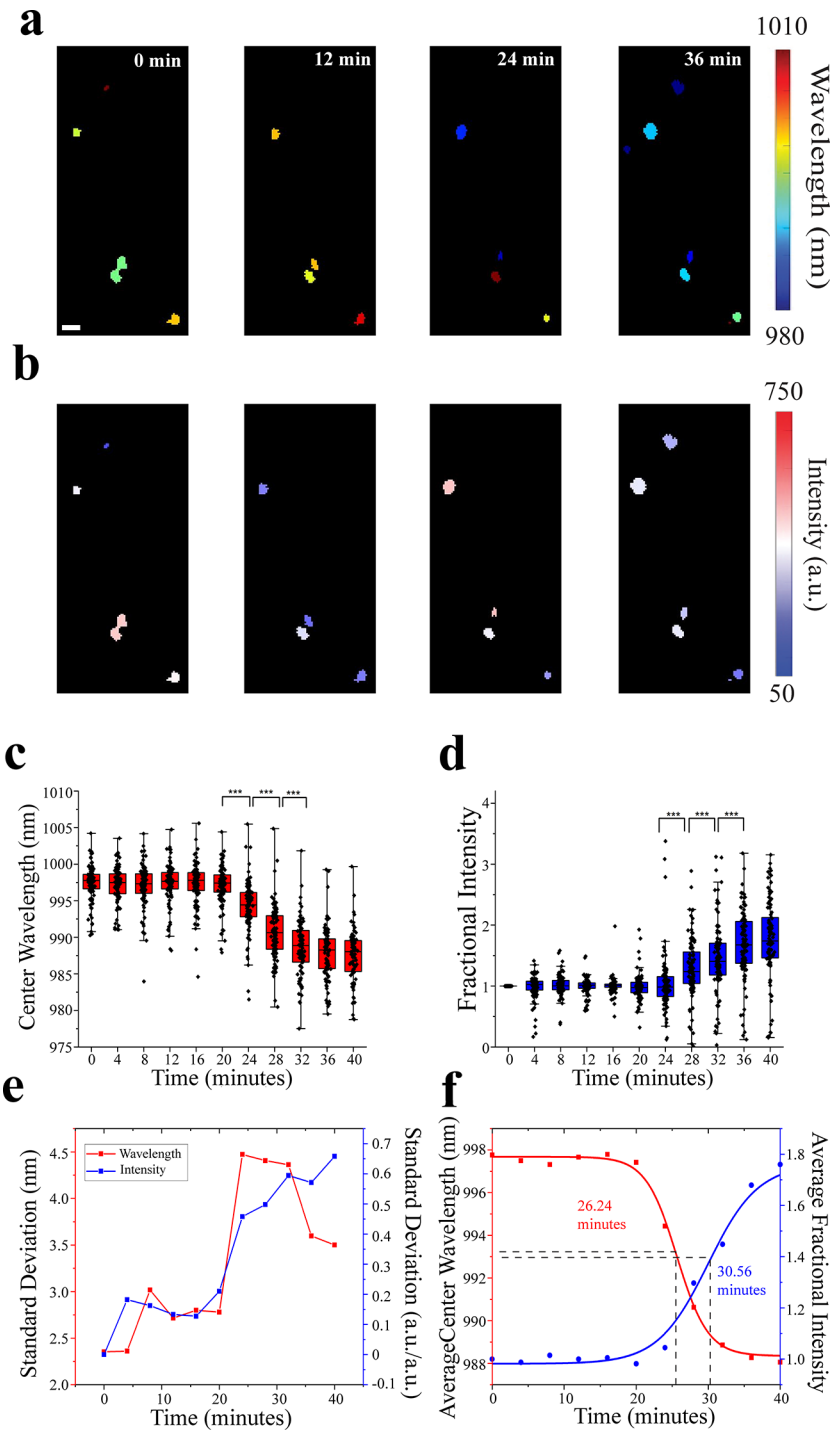

Figure 2. SDC-induced modulations in DNA−SWCNT optical properties. (a) Fitted center emission wavelength and (b) peak fluorescence intensity maps of individual SWCNTs at various times after the addition of 2% SDC. Scale bar is 1 μm. (c) Change in the fitted center wavelength of individual SWCNTs in response to 2% SDC. (d) Change in the peak intensity of individual SWCNTs in response to 2% SDC. Each box contains 25−75% of the data, the middle line represents the median, the open square represents the mean, and the whiskers represent outliers. (e) Standard deviation for both the wavelength and intensity plots. (f) Sigmoidal fits of kinetic data for average emission wavelength (red) and average fractional peak intensity (blue). The time corresponding to the inflection part is indicated for each fit.

their movement is significantly inhibited. However, the platform still allows for conformational changes of the DNA strands on the SWCNT surface. When performing this experiment on glass, a significant portion of the SWCNTs was removed from the glass surface with the addition of SDC (Figure S2). We attribute this to varying electrostatic interactions between the DNA, surfactant, and the charged glass surface. Considering the rapidity of the surfactant exchange mechanism, the initial SDC concentration for analysis of the kinetic response was chosen such that a very low local concentration would be implemented in the layer of SWCNTs in the middle of the hydrogel platform. The thickness of the top hydrogel layer (1.30 mm) was also chosen such that the timescale would be convenient for

https://doi.org/10.1021/acsami.2c16596
ACS Appl. Mater. Interfaces 2023, 15, 1772−1783

hyperspectral fluorescence imaging (i.e., preventing the exchange occurring within a single hyperspectral cube; see Materials and Methods).

We next employed the hydrogel platform with NIR hyperspectral microscopy to investigate the spectral response of individual DNA-SWCNTs during the process of surfactant exchange. First, "hyperspectral cubes" of NIR fluorescence emission from 950 to 1050 nm were acquired (Figure S3). A custom MATLAB code was used to sequentially select regions of interest (ROIs) in each cube, presumably selecting single SWCNTs, and then fit each ROI using a Lorentzian fit. It is important to note that the pixel size of our detector is 150 nm with a 100× objective, which is well below the optical diffraction limit of SWCNTs at about 500 nm.[39] This means that the spectral data are blurred across at least 3 pixels. Spatially resolved maps of emission center wavelength and peak intensity were created to visually demonstrate the evolution of each SWCNT in time (Figure 2a,b and Movies S1 and S2). Overall, the emission center wavelength of each SWCNT seems to blue-shift over a period of 36 min (Figure 2a). However, there is also a slight red shift in the emission wavelength of some individual SWCNTs. Similarly, in Figure 2b although the intensity of each SWCNT primarily increases, there is a small quenching effect seen at the 12 and 36 min time points. There are two possible mechanisms for these observed modulations in wavelength and intensity: either the local heating effect from the laser causes conformational changes of DNA oligonucleotides on the SWCNT surface,[59] or the heating from the laser allows oxygen to bind to the nanotube surface which decreases the exciton binding energy.[17] Of the two mechanisms, the latter is more likely given the linear change in wavelength/intensity over time. If the laser caused conformational changes, it would likely reach some more stable state, but the intensity continues to decrease over time, indicating quenching caused by an increase in the amount of oxygen adsorbed to the surface. Regardless of the mechanism, the red shift and quenching observed are strictly dependent on the laser exposure time and power. Although high laser fluence has been linked to a reduction in quantum yield (QL) previously,[59] lower laser fluence makes it harder to resolve the same individual SWCNTs over time due to the significant decrease in QL or overall intensity. Therefore, the laser power was kept at its maximum in order to fully resolve individual SWCNTs over a long period of time (at least 1 h of continuous excitation).

The emission center wavelength and fractional peak intensity of 100 individual SWCNTs were extracted at each time point, and then plotted as a function of time. To mitigate any negative effects of laser exposure on the SWCNTs, a baseline correction was found and applied to both center wavelength and intensity measurements (Figures S4 and S5). The average delta wavelength (final − initial emission wavelength) was first compared to that of two controls to confirm surfactant exchange. The average delta wavelength after 40 min was 9.7 nm and the final wavelength was 988.1 nm ± 3.5 nm. In solution (Figure S6), the values were 9.9 nm and 986.9 ± 0.4 nm, and in a "bulk" hydrogel (Figure S7), the values were 9.6 and 990.8, respectively (for 2% SDC). The "bulk" hydrogel was prepared by mixing SWCNTs evenly in a PEG-DA hydrogel and then fully crosslinking. Overall, the delta wavelength value was very close to that of both the solution-phase and the "bulk" hydrogel, so we concluded that the SWCNTs are being fully exchanged even in the hydrogel.

The resulting distribution in SWCNT center wavelengths in the spin-coated hydrogel shows little to no response for the first 20 min (Figure 2c), where it then starts to rapidly decline from 20 to 24 min, which was determined to be the first statistically significant change in center wavelength. The intensity does not show a significant change until 28 min (Figure 2d). Thus, the intensity response is delayed by ∼4 min. Figure 2e shows the normalized standard deviation of each plot. Strikingly, the standard deviation of the peak intensity plot increases at the same point as the center wavelength plot (24 min), even though there is no significant increase in the intensity. Sigmoidal fits were made for the average response of both emission wavelength and peak intensity (Figure 2f), and the delay in the intensity response was determined to be exactly 4.32 min by examining the inflection point in the response of each. The delay in the intensity response could indicate that center wavelength and peak intensity are predictors of different phenomena. Although the intensity response is clearly delayed, as noted above, the standard deviation increases at the same time as the standard deviation of the wavelength response. Additionally, the standard deviation of the intensity response continues to increase, while the standard deviation of the wavelength response sharply drops at 32 min. Overall, this combined increase in standard deviation and delay in the intensity response suggest a different mechanism of fluorescence intensity enhancement than with shifts in emission center wavelength.

We also compared the effect of surfactant exchange on DNA-SWCNTs in solution to examine if the delay in the intensity response in our platform could be attributed to laser exposure or is intrinsic to the PEG-DA hydrogel matrix. The inflection point of the peak intensity response occurred about 48.6 s later than that of the wavelength response in the solution phase (Figure S6). A similar effect has also been demonstrated using a probe instrument with a shorter time resolution.[9] We attribute this difference between the solution and the hydrogel to the extremely fast timescale at which the surfactant exchange occurs in solution, as well as the limited resolution in SDC concentration and time when acquiring hyperspectral data. In order to properly compare solution-phase data and the spin-coated hydrogel platform given the vast difference in the kinetic responses, we employed a "bulk" hydrogel as previously mentioned (Figure S7). Similarly, the intensity demonstrated a delay of at least 4 min, even when varying the SDC concentration. The delay in the "bulk" hydrogel varied from 8.56 to 23.28 min. We note that the surfactant exchange response is likely highly dependent on the ratio between the concentration of SWCNTs and SDC in the hydrogel. The reason for the significant difference from the spin-coated hydrogel is due to the increase in SWCNT concentration. There are not enough surfactant molecules to quickly exchange with all of the SWCNTs in the entire hydrogel. Since the delay is repeated in systems where laser exposure has a significantly lower effect, we can rule out the effects of laser exposure and of variations in the local environment due to the hydrogel as a major contributor to this decoupling effect on emission wavelength and peak intensity. Although they clearly play a role in modulating the spectral properties of SWCNTs, the delayed response of the intensity appears to be characteristic of surfactant exchange.

We next used a 1-D diffusion model of SDC through the PEG-DA hydrogel platform to predict the SWCNT response.

https://doi.org/10.1021/acsami.2c16596
ACS Appl. Mater. Interfaces 2023, 15, 1772−1783

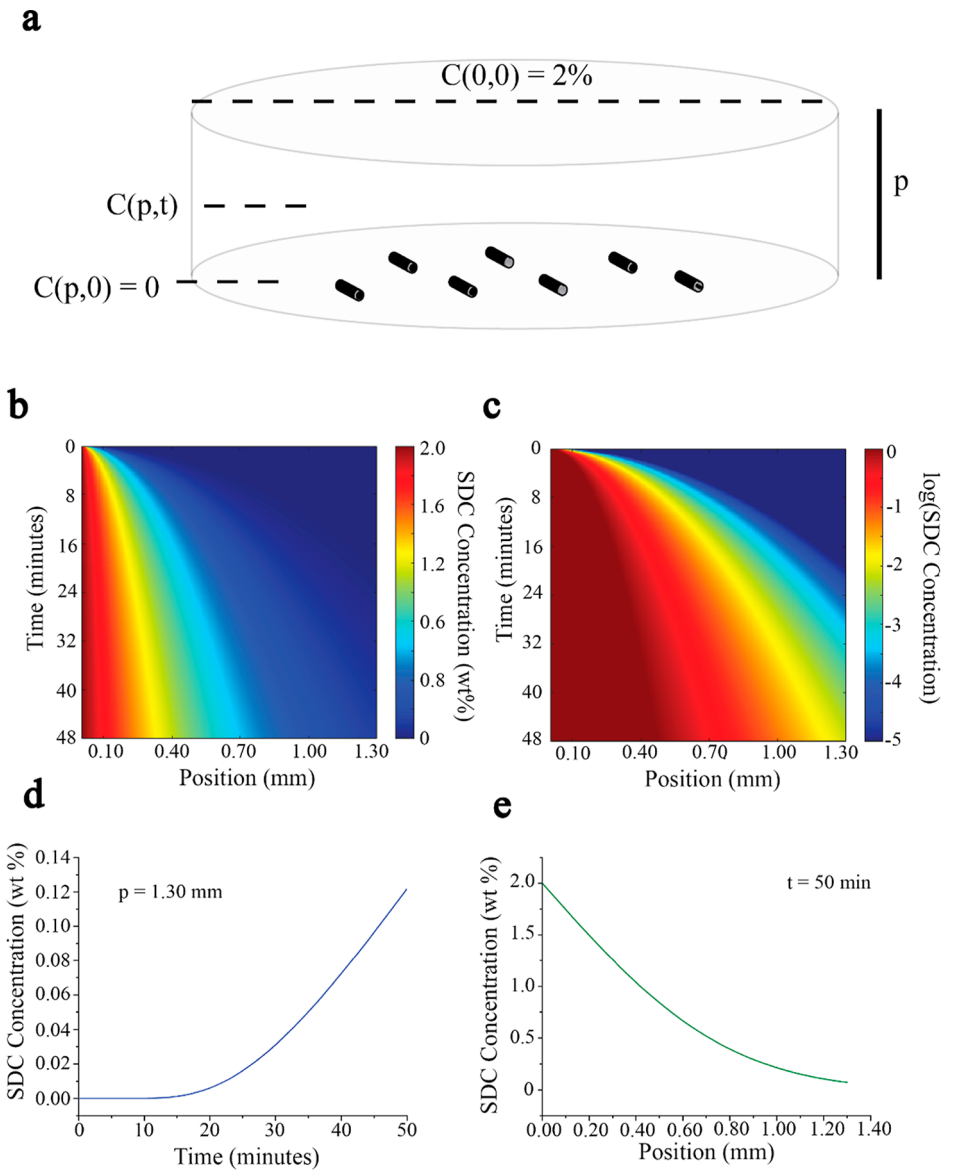

Figure 3. One-dimensional SDC diffusion model in a PEG-DA hydrogel. (a) Schematic representing the boundary and initial conditions and the variables considered. (b,c) Three-dimensional heat maps of position and time vs SDC concentration and log(SDC concentration). (d,e) Concentration profiles of SDC over time and position at defined parameters. The thickness of the hydrogel was determined to be 1.3 mm.

The following boundary and initial conditions were chosen (Figure 3a):

For the concentration at any relevant position and time, $C(p,t)$:

1. $C(0,t) = 2\%$
2. $C(p,0) = 0$
3. $C(\infty,t) = 0$

The concentration of SDC was assumed to be 2% at the top surface of the hydrogel and remained constant over time since the volume of the solution in the glass-bottom dish was sufficiently large. The concentration was then assumed to be 0 at the bottom of the top layer of the hydrogel, where the SWCNTs are located. Finally, the system was modeled as an infinitely long solid, where the concentration at some large distance away from the solution interface at any time is 0. Although we note that the bottom hydrogel layer is relatively thin, since the diffusion of SDC is only tracked over a period of 40 min, we estimate that these boundary conditions are reasonable for our system.

By using Fick's second law of diffusion

$$\frac{\partial c(p,\,t)}{\partial t} = -\frac{\partial J}{\partial p} = D\frac{\partial^2 c}{\partial p^2} \tag{5}$$

where D is the diffusivity of an analyte in a specific medium, p is the position in the medium, t is the time of diffusion, and c is the concentration of the analyte. We then apply the proposed boundary conditions to formulate an equation for the concentration of SDC at any position and time.

We obtain

$$c(p,\,t) = 2 - 2\ \mathrm{erf}\left(\frac{p}{2\sqrt{Dt}}\right) \tag{6}$$

The mesh size (14 nm) was then utilized to find the diffusivity of SDC in the PEG-DA hydrogel using the following equation[60]

https://doi.org/10.1021/acsami.2c16596
ACS Appl. Mater. Interfaces 2023, 15, 1772−1783

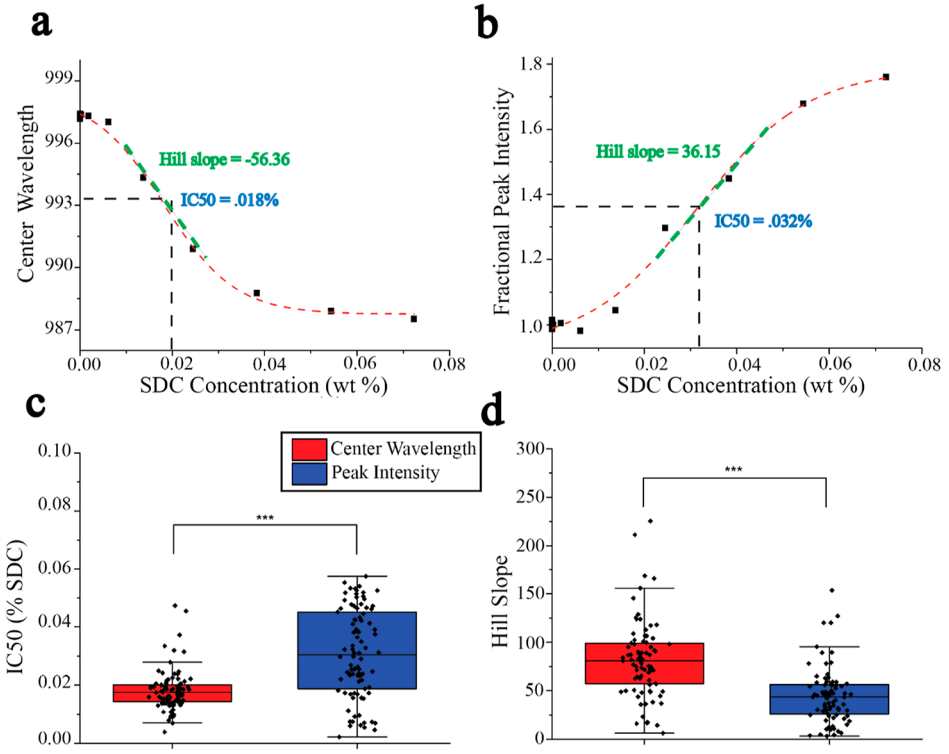

Figure 4. Fitting individual SWCNT modulations to dose−response curves for the analysis of analyte response. (a) Center wavelength and (b) peak intensity dose−response fits of a single representative SWCNT. Comparisons of (c) IC50 and (d) Hill slope values for individual SWCNTs fitted with center wavelength or peak intensity. Each box contains 25−75% of the data, the middle line represents the median, the open square represents the mean, and the whiskers represent outliers. A two-sample *t*-test at 95% confidence was performed to demonstrate significance. (***) significance is denoted by a p-value < 0.001.

$$\frac{D_g}{D_0} = \left(1 - \frac{r_s}{\xi}\right)\exp\left(-Y\left(\frac{v_2}{1 - v_2}\right)\right) \tag{7}$$

where D_g is the diffusivity of the solute in the gel, D_0 is the diffusivity of the solute in the aqueous solution, r_s is the hydrodynamic radius of the solute, ξ is the mesh size of the gel, and Y (approximated as unity) is a ratio of the critical volume required for the translational movement of the solute to the average free volume per molecule of the solvent.[60] The diffusion properties of SDC in solution depend highly on ionic strength, temperature, and concentration due to the formation of micelles, so exact values are difficult to obtain.[61,62] The diffusivity was extrapolated based on the hydrodynamic radius, which was estimated to be about 2 nm. An average hydrodynamic radius was assumed since it is expected that the hydrodynamic radius will change as the local concentration of SDC changes in the hydrogel due to modulations in micelle size. The diffusivity of SDC in solution at room temperature was then estimated to be 1.03×10^{-6} cm^2/s from the literature.[62−64] The effective diffusivity of SDC in the gel was determined to be 23% lower than that in solution using eq 7 or 8.02×10^{-7} cm^2/s which is close to the diffusivity of solute particles with a similar hydrodynamic radius in a PEG-DA hydrogel.[63]

Two-dimensional heat maps of SDC concentration in the hydrogel at position p and time t were then created using MATLAB (Figure 3b,c). The position for each ranged from p = 0−0.13 cm, which is the distance from the top of the swelled hydrogel to the layer of SWCNTs. Each heat map therefore shows the concentration of SDC in the hydrogel platform from the surface to the layer of SWCNTs over a 50 min period. Concentration profiles were extracted from these heat maps (Figure 3d,e) to show the profile at a defined position or time. This model allows for the prediction of the concentration of SDC at any position and time, which can be used to estimate the local concentration of SDC at the surface of a single SWCNT.

Individual SWCNT dose−response curves were created in order to further investigate the differences and heterogeneity in center wavelength and peak intensity of SDC-induced DNA-to-surfactant exchange. Utilizing the modeled data from Figure 3d, dose−response curves were created for each individual SWCNT (n = 100) by converting the x-axis from time to concentration. Each individual SWCNT was fit using a version of the Hill equation

$$y = A1 + \frac{(A2 - A1)}{1 + 10^{\log(IC50) - x*H}} \tag{8}$$

where y is the response (λ), $A1$ is the minimum response value, $A2$ is the maximum response value, IC50 is the concentration that produces 50% of the maximal response, x is the concentration, and H is the Hill slope. The Hill slope generally corresponds to the degree of cooperative binding between the substrate and analyte.[65,66] In this context, it describes the interactions between DNA, surfactant molecules, and the SWCNT sidewall. Sample dose−response fits are shown in Figure 4a,b. In this case, the IC50 value corresponds to the concentration at which 50% of the corresponding optical property shifts to its final value. The IC50 and Hill slopes for the wavelength and intensity fits for 100 ROIs were then extracted and box and whisker plots were created (Figure 4c,d). The average IC50 value for the peak intensity of

https://doi.org/10.1021/acsami.2c16596
ACS Appl. Mater. Interfaces 2023, 15, 1772−1783

individual SWCNTs, 0.031 ± 0.015%, was significantly larger ($p < 0.001$) than the average IC50 value for the center wavelength, 0.018 ± 0.0064%. The Hill coefficient of each SWCNT was also compared and revealed significance between peak intensity (44.84 ± 28.88) and center wavelength (81.74 ± 39.65), ($p < 0.01$). The IC50 values for both the wavelength and intensity dose−response curves are larger than that of the solution-phase data, which indicates that the exchange with SDC occurs at a much higher surfactant concentration in the hydrogel (Figures S8 and S9). We note that the presence of surfactant interactions with individual polymer chains in the hydrogel and modulations in hydrodynamic size are potentially major contributors.

Given the finding that the IC50 of the center wavelength response for individual SWCNTs in the platform is significantly lower than the IC50 of peak intensity, this demonstrates that the center wavelength response occurs at a lower SDC concentration. Essentially, less surfactant molecules are required to maximally shift the center wavelength of each SWCNT than the peak intensity of each SWCNT. However, additional surfactant molecules still cause the peak intensity to increase. The low standard deviation between the IC50 values of individual wavelength dose−response fits supports the idea that given the SWCNT full exchanges, the process is largely independent of variations in local concentration or physical characteristics of each SWCNT. The peak intensity is then highly dependent on both the number and specific morphology of SDC molecules on the SWCNT surface, given the strikingly large variation between individual SWCNTs. Emission center wavelength is therefore a better predictor of the overall conformational state of a SWCNT during surfactant exchange (i.e., DNA−SWCNT vs half-exchanged DNA−SWCNT vs SDC-SWCNT). The large degree of variation in the Hill slope of the wavelength response shows that the rate of the exchange is likely concentration-dependent. The larger value of the Hill slope for the wavelength fits relative to the intensity fits corresponds to an increase in the cooperative binding between surfactant molecules and the SWCNT surface during the initial surfactant exchange. The distinct difference in the slope likely reveals an intermediate conformation of surfactant molecules on the SWCNT surface that rearrange more slowly than the initial exchange from DNA to SDC indicated by the wavelength response. We hypothesize that the center wavelength response can then determine the degree of surface coverage, where the intensity response is related but ultimately a predictor of different phenomena which can be analyzed by looking at specific parameters.

Although the exact binding mechanism and conformation of SDC molecules on a SWCNT surface have not yet been demonstrated, different theories have been proposed.[67,68] A likely explanation could be that the surfactant molecules have some change in morphology from a hemimicelle structure with less surface coverage to a thicker micelle with full surface coverage. This was briefly examined by adding an extremely high concentration of SDC to immediately observe the surfactant exchange independent of some initial laser exposure (Figure S10). Although the exchange process appears to have been completed, the wavelength and intensity are clearly still modulated by the laser; thus, there is some degree of the SWCNT surface exposed to the environment. We examined this effect of surface coverage on the quenching of SWCNTs by exposing exchanged SDC-SWCNTs in the hydrogel platform (>30 min after the maximum shift) to the laser, where no significant shifts were observed after an additional 20 min (Figure S11). This helps to support the fact that oxygen is adsorbing to the SWCNT surface since the quenching is significantly mitigated depending on the degree of SWCNT surface coverage. Combined with the delay in intensity response relative to the wavelength response, there is clear evidence that there exists some intermediate conformational state that upon an increase in surfactant concentration reorganizes to create a more stable conformation. Although we demonstrate a pathway to understanding individual SWCNT optical properties, extensive modeling will need to be performed in the future to fully describe these effects.

Two-dimensional scatter plots were constructed to investigate potential correlations between various fitted spectral properties of individual SWCNTs undergoing surfactant exchange within the hydrogel platform. For instance, "starting center wavelength" versus "IC50 center wavelength" (Figure S12). Surprisingly, no trends were found, which can be attributed to the large heterogeneity of individual SWCNTs. The standard method to produce dispersed SWCNTs, that is, probe-tip sonication, yields shorter SWCNTs as a function of sonication randomly cutting the SWCNTs in addition to creating defects along the SWCNT sidewall.[14] As a result, there is a heterogeneous length distribution in each SWCNT sample, as well as variations in the number of defects from sample to sample.[14] Due to the diffraction limit and average size of DNA-SWCNTs, we are not able to fully resolve the length. We believe length variations and the presence of defects in a single-chirality solution are among the most significant causes of spectral heterogeneity. We have previously shown heterogeneity in the center wavelength and peak intensity even along single SWCNTs absent of any change in the environment.[39] Recently, long surfactant-coated nanotubes have been created that are remarkably more homogeneous than standard samples, where the intensity is largely dependent on the length.[14] Therefore, we believe that modification of standard SWCNT production procedures may be necessary to carefully control the length and presence of defects, that is, through advanced solution-phase sorting approaches.[69]

CONCLUSIONS

In this study, we investigated the interactions between SDC and individual DNA-SWCNTs as the surfactant rapidly exchanged with the DNA on the SWCNT surface. We immobilized the SWCNTs in a neutral hydrogel platform to investigate their properties in their native aqueous state. Nearly all of the SWCNTs do not move over time in response to SDC but still allow for conformational changes of the functionalization on the SWCNT surface. In order to characterize the response of emission center wavelength and peak fluorescence intensity, wavelength maps and box plots were created with data extracted at intervals of 4 min after the addition of SDC. The center wavelength clearly blue-shifts over time as expected from the solution, and the peak intensity significantly increased but demonstrated a delayed response. We then related this to a 1-D diffusion model to estimate the local concentration of surfactant at the SWCNT surface. We fit the center wavelength and peak intensity response of each individual SWCNT to dose−response curves and confirmed a delay in the intensity response. The high standard deviation of the response was attributed to modulations induced by high laser power. From this, we found that the degree of surface coverage of SWCNTs

https://doi.org/10.1021/acsami.2c16596
ACS Appl. Mater. Interfaces 2023, 15, 1772−1783

clearly affects the heterogeneity of individual SWCNTs and may indicate an intermediate conformation of SDC on the SWCNT surface during the exchange. We hypothesize that the wavelength is a better predictor of surfactant exchange and is directly related to the amount of DNA that is exchanged, whereas the intensity is related but demonstrates a delayed response linked to some reorganization of surfactant molecules. Our platform can thus be used to investigate the kinetics of spectral changes, which can be related to different characteristics such as DNA stability and functionalization morphology. Overall, this research highlights the need for stricter control over standard SWCNT suspensions. However, by investigating individual SWCNTs in their native state, standard ensemble measurements can be improved and true single-molecule measurements can be approached.

MATERIALS AND METHODS

DNA−SWCNT Sample Preparation. Throughout this study, SWCNTs produced using the SG65i CoMoCAT process (Sigma-Aldrich) were used. 1 mg of raw nanotubes was added to 2 mg of ss$(GT)_{15}$ DNA oligonucleotide (Integrated DNA Technologies) and 1 mL of 100 mM NaCl (Sigma-Aldrich). The suspension was then placed in a 0 °C temperature-controlled microcentrifuge holder and ultrasonicated with a 1/8 in. tapered microtip at 40% amplitude for 30 min (Sonics Vibracell VCX-130; Sonics and Materials). The dispersion was then ultracentrifuged (Sorvall Discovery M120 SE) for 30 min at 250,000*g*, and the top 80% of the supernatant was extracted. The concentration of each dispersion was determined using a UV/vis/NIR spectrophotometer (Jasco, Tokyo, Japan) and the extinction coefficient A_{910} = 0.02554 L mg^{-1} cm^{-1}.[70]

Hydrogel Characterization. In order to obtain the thickness of the hydrogel, the top layer was separately soaked in 2 mL of 1× PBS for 4 h. The thickness was then measured with calipers, and a second measurement was taken after soaking it for 20 more hours to confirm that the hydrogel had fully swollen. The top layer of the hydrogel was also weighed after 24 h of soaking and then left in an oven at 37 °C for 48 h. Once the hydrogel was completely dried, it was weighed and the swelling ratio was calculated as a ratio between the dry and wet weights.

PEG Platform Procedure. 400 μL of 3-(trimethoxysilyl)propyl methacrylate (Sigma-Aldrich) was added to 100 mL of acetic acid at a pH of 3.5. To create the platform, 35 mm glass-bottom Petri dishes (MatTek) with a glass diameter of 14 mm were first soaked in 200 μL of the methacrylate solution overnight. 200 μL of 40 wt % 8 kDa poly(ethylene glycol) diacrylate (PEG-DA) (Thermo Scientific) and 140 μL of PBS were then mixed with 60 μL of a photoinitiator, lithium phenyl-2,4,6-trimethylbenzoylphosphinate (LAP) (CelLink), at a concentration of 7 mg/mL. The resulting precursor solution was then deposited onto a functionalized glass-bottom Petri dish. The glass-bottom dish with the PEG-DA precursor solution was then placed onto a spin-coater (Laurell Model WS-400BZ-6NPP/LITE), where the lid was closed and a small 365 nm UV lamp was positioned over a small opening on the lid. The samples were then spun at 0 rpm for 20 s and then in increments of 200 rpm for 10 s until 1200 rpm was reached, all the while the UV lamp was on. The sample was then left to fully UV cure for 10 min. After the bottom layer of the hydrogel was fully crosslinked, it was lightly washed with PBS. A separate layer of the PEG-DA hydrogel was prepared in another 35 mm glass-bottom dish with a 10 mm coverslip by placing a coverslip over the small opening with 150 μL of the precursor solution and then UV curing in a similar manner. Simultaneously, 100 μL of a 2 mg/L DNA−SWCNT solution was spin-coated onto the bottom hydrogel layer at 1200 rpm. The second layer was then carefully placed on top of the PEG-DA layer with SWCNTs and then crosslinked to the bottom layer under a UV lamp for 20 min. 50 μL of an excess PEG-DA/LAP solution was placed around the seam of the two layers and then allowed to crosslink via UV exposure for 15 min. The hydrogel was washed three times with PBS (10 min for each wash), and then 2 mL of PBS was added to the MatTek to allow the hydrogel to swell. The hydrogel was washed to remove any free DNA or excess radicals present in the hydrogel. The "bulk" hydrogel was prepared by first adding 20 μL of 25 mg/L DNA-SWCNTs to 50 μL of 40% PEG-DA, 10 μL of the photoinitiator (7 mg/mL), and 20 μL of PBS. 50 μL of the precursor solution was placed into a 35 mm MatTek with a glass diameter of 14 mm and the solution was subsequently crosslinked under a UV lamp for 10 min. The sample was then submerged in varying amounts of PBS depending on the volume of SDC that was later added.

Near-Infrared Fluorescence Microscopy. Near-infrared spectra were acquired from individual SWCNTs by using a NIR hyperspectral fluorescence microscope, similar to a previously described system.[39] The hydrogel sample was mounted onto the stage of an Olympus 1X-73 inverted microscope, where a 730 nm diode laser (1.5 W) was reflected onto the sample using a UApo N 100×/1.49 oil immersion objective (Olympus, U.S.A). Stacks of spectral images were acquired by passing the emission through a volume Bragg Grating and subsequently collecting it with a 2d InGaAs array detector (photon, etc.). Stacks of spectral images, "hyperspectral cubes" were acquired for each sample using standard conditions (wavelength range: 950−1050 nm, stepping size: 4 nm, exposure time: 1.2 s). A cube was automatically acquired every 4 min by using a custom PhySpec sequence. 400 μL of a solution of 12% SDC (Sigma-Aldrich) was added 45 min after the sample was exposed to the 730 nm laser at an exposure time of 1 s, and the first cube was immediately taken. For the measurement of spectral modulations independent of initial laser exposure, data was acquired 30 min after the removal of PBS and subsequent addition of 6% SDC. Solution spectra were acquired by adding a solution of DNA-SWCNTs to a 96-well plate at a concentration of 2 mg/L in each of the 30 wells with a working volume of 200 μL. Six different SDC concentrations were tested. The 96-well plate was mounted on the hyperspectral microscope, and a 20× objective was used. A custom PhySpec sequence was created to automatically scan and acquire hyperspectral cubes (wavelength range: 950−1050 nm, stepping size: 2 nm, exposure time: 0.6 s) from each well.

Spectral Analysis. Spectra were fitted to either a Lorentzian (single SWCNT) or Gaussian (solution/"bulk" spectra) curve using OriginPro 2019 and custom MATLAB codes to obtain the center wavelength and peak intensity. Once the fitted spectral properties were obtained, spectral maps were created in MATLAB. In order to subtract the effect of laser exposure from the spectra of each SWCNT, a linear fit (OriginPro) for both wavelength and intensity was created for each individual SWCNT for the first 16 min before the exchange occurred. This was then extrapolated to 40 min and subtracted from the spectra of the same individual SWCNT.

Statistical Analysis. All statistical analysis was completed in OriginPro 2019. Significance was determined using a two-sample *t*-test under the null hypothesis. Figures for the 1-D diffusion model were all plotted in MATLAB, and image analysis was performed using Image J software.

ASSOCIATED CONTENT

Supporting Information

The Supporting Information is available free of charge at https://pubs.acs.org/doi/10.1021/acsami.2c16596.

Broadband images of SWCNT surfactant exchange on glass, raw fluorescence spectra in the hydrogel, laser-induced SWCNT modulations, solution-phase surfactant exchange spectra, bulk hydrogel spectra, dose−response fits in solution, laser-induced modulations after surfactant exchange, laser-induced modulations on SDC-SWCNTs, and various scatter plots of selected optical properties (PDF)

NIR fluorescence emission wavelength of individual SWCNTs after the addition of SDC (AVI)

https://doi.org/10.1021/acsami.2c16596
ACS Appl. Mater. Interfaces 2023, 15, 1772−1783

NIR fluorescence peak intensity of individual SWCNTs after the addition of SDC (AVI)

AUTHOR INFORMATION

Corresponding Author

Daniel Roxbury − *Department of Chemical Engineering, University of Rhode Island, Kingston, Rhode Island 02886, United States;* orcid.org/0000-0003-2812-3523; Email: roxbury@uri.edu

Authors

Matthew Card − *Department of Chemical Engineering, University of Rhode Island, Kingston, Rhode Island 02886, United States;* orcid.org/0000-0002-0471-0961

Raisa Alejandro − *Department of Chemical Engineering, University of Rhode Island, Kingston, Rhode Island 02886, United States*

Complete contact information is available at: https://pubs.acs.org/10.1021/acsami.2c16596

Notes

The authors declare no competing financial interest.

ACKNOWLEDGMENTS

This work was supported by the National Science Foundation (CAREER Award #1844536, # 2231621, and EPSCoR, Cooperative Agreement #OIA-1655221) and the University of Rhode Island College of Engineering. Research was made possible by the use of equipment available through the Rhode Island Institutional Development Award (IDeA) Network of Biomedical Research Excellence from the National Institute of General Medical Sciences of the National Institutes of Health under grant #P20GM103430 through the Centralized Research Core facility.

REFERENCES

(1) Farrera, C.; Torres Andón, F.; Feliu, N. Carbon Nanotubes As Optical Sensors In Biomedicine. *ACS Nano* **2017**, *11*, 10637−10643.

(2) Thostenson, E. T.; Ren, Z.; Chou, T.-W. Advances In The Science And Technology Of Carbon Nanotubes And Their Composites: A Review. *Compos. Sci. Technol.* **2001**, *61*, 1899−1912.

(3) Adhikari, B.-R.; Govindhan, M.; Chen, A. Carbon Nanomaterials Based Electrochemical Sensors/Biosensors For The Sensitive Detection Of Pharmaceutical And Biological Compounds. *Sensors* **2015**, *15*, 22490−22508.

(4) O'Connell, M. J.; Bachilo, S. M.; Huffman, C. B.; Moore, V. C.; Strano, M. S.; Haroz, E. H.; Rialon, K. L.; Boul, P. J.; Noon, W. H.; Kittrell, C.; Ma, J.; Hauge, R. H.; Weisman, R. B.; Smalley, R. E. Band Gap Fluorescence From Individual Single-Walled Carbon Nanotubes. *Science* **2002**, *297*, 593−596.

(5) Maultzsch, J.; Pomraenke, R.; Reich, S.; Chang, E.; Prezzi, D.; Ruini, A.; Molinari, E.; Strano, M. S.; Thomsen, C.; Lienau, C. Exciton Binding Energies In Carbon Nanotubes From Two-Photon Photoluminescence. *Phys. Rev. B: Condens. Matter Mater. Phys.* **2005**, *72*, 241402.

(6) Boghossian, A. A.; Zhang, J.; Barone, P. W.; Reuel, N. F.; Kim, J. H.; Heller, D. A.; Ahn, J. H.; Hilmer, A. J.; Rwei, A.; Arkalgud, J. R.; Zhang, C. T.; Strano, M. S. Near-Infrared Fluorescent Sensors Based On Single-Walled Carbon Nanotubes For Life Sciences Applications. *Chemsuschem* **2011**, *4*, 848−863.

(7) Kruss, S.; Landry, M. P.; Vander Ende, E.; Lima, B. M.; Reuel, N. F.; Zhang, J.; Nelson, J.; Mu, B.; Hilmer, A.; Strano, M. Neurotransmitter Detection Using Corona Phase Molecular Recognition On Fluorescent Single-Walled Carbon Nanotube Sensors. *J. Am. Chem. Soc.* **2014**, *136*, 713−724.

(8) Bisker, G.; Dong, J.; Park, H. D.; Iverson, N. M.; Ahn, J.; Nelson, J. T.; Landry, M. P.; Kruss, S.; Strano, M. S. Protein-Targeted Corona Phase Molecular Recognition. *Nat. Commun.* **2016**, *7*, 10241.

(9) Jena, P. V.; Safaee, M. M.; Heller, D. A.; Roxbury, D. DNA-Carbon Nanotube Complexation Affinity And Photoluminescence Modulation Are Independent. *ACS Appl. Mater. Interfaces* **2017**, *9*, 21397−21405.

(10) Freeley, M.; Attanzio, A.; Cecconello, A.; Amoroso, G.; Clement, P.; Fernandez, G.; Gesuele, F.; Palma, M. Tuning The Coupling In Single-Molecule Heterostructures: DNA-Programmed And Reconfigurable Carbon Nanotube-Based Nanohybrids. *Adv. Sci.* **2018**, *5*, 1800596.

(11) Peng, R.; Tang, X. S.; Li, D. Detection Of Individual Molecules And Ions By Carbon Nanotube-Based Differential Resistive Pulse Sensor. *Small* **2018**, *14*, No. E1800013.

(12) Gravely, M.; Safaee, M. M.; Roxbury, D. Biomolecular Functionalization Of A Nanomaterial To Control Stability And Retention Within Live Cells. *Nano Lett.* **2019**, *19*, 6203−6212.

(13) Galassi, T. V.; Antman-Passig, M.; Yaari, Z.; Jessurun, J.; Schwartz, R. E.; Heller, D. A. Long-Term In Vivo Biocompatibility Of Single-Walled Carbon Nanotubes. *PLoS One* **2020**, *15*, No. E0226791.

(14) Safaee, M. M.; Gravely, M.; Rocchio, C.; Simmeth, M.; Roxbury, D. DNA Sequence Mediates Apparent Length Distribution In Single-Walled Carbon Nanotubes. *ACS Appl. Mater. Interfaces* **2019**, *11*, 2225−2233.

(15) Roxbury, D.; Tu, X.; Zheng, M.; Jagota, A. Recognition Ability Of DNA For Carbon Nanotubes Correlates With Their Binding Affinity. *Langmuir* **2011**, *27*, 8282−8293.

(16) Ao, G.; Streit, J. K.; Fagan, J. A.; Zheng, M. Differentiating Left- And Right-Handed Carbon Nanotubes By DNA. *J. Am. Chem. Soc.* **2016**, *138*, 16677−16685.

(17) Zheng, Y.; Bachilo, S. M.; Weisman, R. B. Quenching Of Single-Walled Carbon Nanotube Fluorescence By Dissolved Oxygen Reveals Selective Single-Stranded DNA Affinities. *J. Phys. Chem. Lett.* **2017**, *8*, 1952−1955.

(18) Alizadehmojarad, A. A.; Zhou, X.; Beyene, A. G.; Chacon, K. E.; Sung, Y.; Pinals, R. L.; Landry, M. P.; Vuković, L. Binding Affinity And Conformational Preferences Influence Kinetic Stability Of Short Oligonucleotides On Carbon Nanotubes. *Adv. Mater. Interfaces* **2020**, *7*, 2000353.

(19) Roxbury, D.; Mittal, J.; Jagota, A. Molecular-Basis Of Single-Walled Carbon Nanotube Recognition By Single-Stranded DNA. *Nano Lett.* **2012**, *12*, 1464−1469.

(20) Oh, H.; Sim, J.; Ju, S.-Y. Binding Affinities And Thermodynamics Of Noncovalent Functionalization Of Carbon Nanotubes With Surfactants. *Langmuir* **2013**, *29*, 11154−11162.

(21) Subbaiyan, N. K.; Cambré, S.; Parra-Vasquez, A. N. G.; Hároz, E. H.; Doorn, S. K.; Duque, J. G. Role Of Surfactants And Salt In Aqueous Two-Phase Separation Of Carbon Nanotubes Toward Simple Chirality Isolation. *ACS Nano* **2014**, *8*, 1619−1628.

(22) Jena, P. V.; Roxbury, D.; Galassi, T. V.; Akkari, L.; Horoszko, C. P.; Iaea, D. B.; Budhathoki-Uprety, J.; Pipalia, N.; Haka, A. S.; Harvey, J. D.; Mittal, J.; Maxfield, F. R.; Joyce, J. A.; Heller, D. A. A Carbon Nanotube Optical Reporter Maps Endolysosomal Lipid Flux. *ACS Nano* **2017**, *11*, 10689−10703.

(23) Gong, X.; Shuai, L.; Beingessner, R. L.; Yamazaki, T.; Shen, J.; Kuehne, M.; Jones, K.; Fenniri, H.; Strano, M. S. Size Selective Corona Interactions From Self-Assembled Rosette And Single-Walled Carbon Nanotubes. *Small* **2022**, *18*, 2104951.

(24) Wenseleers, W.; Vlasov, I. I.; Goovaerts, E.; Obraztsova, E. D.; Lobach, A. S.; Bouwen, A. Efficient Isolation And Solubilization Of Pristine Single-Walled Nanotubes In Bile Salt Micelles. *Adv. Funct. Mater.* **2004**, *14*, 1105−1112.

(25) Hilmer, A. J.; McNicholas, T. P.; Lin, S.; Zhang, J.; Wang, Q. H.; Mendenhall, J. D.; Song, C.; Heller, D. A.; Barone, P. W.; Blankschtein, D.; Strano, M. S. Role Of Adsorbed Surfactant In The Reaction Of Aryl Diazonium Salts With Single-Walled Carbon Nanotubes. *Langmuir* **2012**, *28*, 1309−1321.

(26) Salem, D. P.; Gong, X.; Liu, A. T.; Koman, V. B.; Dong, J.; Strano, M. S. Ionic Strength-Mediated Phase Transitions Of Surface-Adsorbed DNA On Single-Walled Carbon Nanotubes. *J. Am. Chem. Soc.* **2017**, *139*, 16791−16802.
(27) Chiu, C. F.; Dar, H. H.; Kapralov, A. A.; Robinson, R. A.; Kagan, V. E.; Star, A. Nanoemitters And Innate Immunity: The Role Of Surfactants And Bio-Coronas In Myeloperoxidase-Catalyzed Oxidation Of Pristine Single-Walled Carbon Nanotubes. *Nanoscale* **2017**, *9*, 5948−5956.
(28) Gravely, M.; Kindopp, A.; Hubert, L.; Card, M.; Nadeem, A.; Miller, C.; Roxbury, D. Aggregation Reduces Subcellular Localization And Cytotoxicity Of Single-Walled Carbon Nanotubes. *ACS Appl. Mater. Interfaces* **2022**, *14*, 19168.
(29) Koh, B.; Cheng, W. Mechanisms Of Carbon Nanotube Aggregation And The Reversion Of Carbon Nanotube Aggregates In Aqueous Medium. *Langmuir* **2014**, *30*, 10899−10909.
(30) Jin, H.; Heller, D. A.; Kalbacova, M.; Kim, J.-H.; Zhang, J.; Boghossian, A. A.; Maheshri, N.; Strano, M. S. Detection Of Single-Molecule H 2 O 2 Signalling From Epidermal Growth Factor Receptor Using Fluorescent Single-Walled Carbon Nanotubes. *Nat. Nanotechnol.* **2010**, *5*, 302−309.
(31) Hong, T.; Wang, T.; Xu, Y.-Q. Direct Measurement Of Π Coupling At The Single-Molecule Level Using A Carbon Nanotube Force Sensor. *Nano Lett.* **2018**, *18*, 7883−7888.
(32) Macchia, E.; Torricelli, F.; Bollella, P.; Sarcina, L.; Tricase, A.; Di Franco, C.; Österbacka, R.; Kovács-Vajna, Z. M.; Scamarcio, G.; Torsi, L. Large-Area Interfaces For Single-Molecule Label-Free Bioelectronic Detection. *Chem. Rev.* **2022**, *122*, 4636−4699.
(33) Landry, M. P.; Ando, H.; Chen, A. Y.; Cao, J.; Kottadiel, V. I.; Chio, L.; Yang, D.; Dong, J.; Lu, T. K.; Strano, M. S. Single-Molecule Detection Of Protein Efflux From Microorganisms Using Fluorescent Single-Walled Carbon Nanotube Sensor Arrays. *Nat. Nanotechnol.* **2017**, *12*, 368−377.
(34) Qu, H.; Rayabharam, A.; Wu, X.; Wang, P.; Li, Y.; Fagan, J.; Aluru, N. R.; Wang, Y. Selective Filling Of N-Hexane In A Tight Nanopore. *Nat. Commun.* **2021**, *12*, 310.
(35) Thrift, W. J.; Ragan, R. Quantification Of Analyte Concentration In The Single Molecule Regime Using Convolutional Neural Networks. *Anal. Chem.* **2019**, *91*, 13337−13342.
(36) Kneipp, K.; Wang, Y.; Kneipp, H.; Perelman, L. T.; Itzkan, I.; Dasari, R. R.; Feld, M. S. Single Molecule Detection Using Surface-Enhanced Raman Scattering (SERS). *Phys. Rev. Lett.* **1997**, *78*, 1667.
(37) Liu, X.; Pichler, T.; Knupfer, M.; Golden, M.; Fink, J.; Kataura, H.; Achiba, Y. Detailed Analysis Of The Mean Diameter And Diameter Distribution Of Single-Wall Carbon Nanotubes From Their Optical Response. *Phys. Rev. B: Condens. Matter Mater. Phys.* **2002**, *66*, 045411.
(38) Graf, A.; Zakharko, Y.; Schießl, S. P.; Backes, C.; Pfohl, M.; Flavel, B. S.; Zaumseil, J. Large Scale, Selective Dispersion Of Long Single-Walled Carbon Nanotubes With High Photoluminescence Quantum Yield By Shear Force Mixing. *Carbon* **2016**, *105*, 593−599.
(39) Card, M.; Gravely, M.; Madani, S. M. Z.; Roxbury, D. A Spin-Coated Hydrogel Platform Enables Accurate Investigation Of Immobilized Individual Single-Walled Carbon Nanotubes. *ACS Appl. Mater. Interfaces* **2021**, *13*, 31986−31995.
(40) Ahmed, E. M. Hydrogel: Preparation, Characterization, And Applications: A Review. *J. Adv. Res.* **2015**, *6*, 105−121.
(41) Salehi, A. A.; Ghannadi-Maragheh, M.; Torab-Mostaedi, M.; Torkaman, R.; Asadollahzadeh, M. Hydrogel Materials As An Emerging Platform For Desalination And The Production Of Purified Water. *Sep. Purif. Rev.* **2021**, *50*, 380−399.
(42) Larrañeta, E.; Stewart, S.; Ervine, M.; Al-Kasasbeh, R.; Donnelly, R. F. Hydrogels For Hydrophobic Drug Delivery. Classification, Synthesis And Applications. *J. Funct. Biomater.* **2018**, *9*, 13.
(43) Vashist, A.; Kaushik, A.; Vashist, A.; Sagar, V.; Ghosal, A.; Gupta, Y.; Ahmad, S.; Nair, M. Advances In Carbon Nanotubes−Hydrogel Hybrids In Nanomedicine For Therapeutics. *Adv. Healthcare Mater.* **2018**, *7*, 1701213.
(44) Bakh, N. A.; Gong, X.; Lee, M. A.; Jin, X.; Koman, V. B.; Park, M.; Nguyen, F. T.; Strano, M. S. Transcutaneous Measurement of Essential Vitamins Using Near-Infrared Fluorescent Single-Walled Carbon Nanotube Sensors. *Small* **2021**, *17*, 2100540.
(45) Mansukhani, N. D.; Guiney, L. M.; Wei, Z.; Roth, E. W.; Putz, K. W.; Luijten, E.; Hersam, M. C. Optothermally Reversible Carbon Nanotube−DNA Supramolecular Hybrid Hydrogels. *Macromol. Rapid Commun.* **2018**, *39*, 1700587.
(46) Nißler, R.; Bader, O.; Dohmen, M.; Walter, S. G.; Noll, C.; Selvaggio, G.; Groß, U.; Kruss, S. Remote Near Infrared Identification of Pathogens with Multiplexed Nanosensors. *Nat. Commun.* **2020**, *11*, 5995.
(47) Rahimi Mamaghani, K.; Morteza Naghib, S.; Zahedi, A.; Mozafari, M. Synthesis and Microstructural Characterization of Gelma/PEGDA Hybrid Hydrogel Containing Graphene Oxide for Biomedical Purposes. *Mater. Today: Proc.* **2018**, *5*, 15635−15644.
(48) Warr, C.; Valdoz, J. C.; Bickham, B. P.; Knight, C. J.; Franks, N. A.; Chartrand, N.; Van Ry, P. M.; Christensen, K. A.; Nordin, G. P.; Cook, A. D. Biocompatible PEGDA Resin for 3D Printing. *ACS Appl. Bio Mater.* **2020**, *3*, 2239−2244.
(49) Wei, X.; Tanaka, T.; Hirakawa, T.; Wang, G.; Kataura, H. High-Efficiency Separation of (6, 5) Carbon Nanotubes by Stepwise Elution Gel Chromatography. *Phys. Status Solidi B* **2017**, *254*, 1700279.
(50) Nißler, R.; Mann, F. A.; Chaturvedi, P.; Horlebein, J.; Meyer, D.; Vuković, L.; Kruss, S. Quantification of The Number of Adsorbed DNA Molecules on Single-Walled Carbon Nanotubes. *J. Phys. Chem. C* **2019**, *123*, 4837−4847.
(51) Safaee, M. M.; Gravely, M.; Lamothe, A.; McSweeney, M.; Roxbury, D. Enhancing the Thermal Stability of Carbon Nanomaterials with DNA. *Sci. Rep.* **2019**, *9*, 11926.
(52) Dave, N.; Chan, M. Y.; Huang, P.-J. J.; Smith, B. D.; Liu, J. Regenerable DNA-Functionalized Hydrogels for Ultrasensitive, Instrument-Free Mercury(II) Detection and Removal in Water. *J. Am. Chem. Soc.* **2010**, *132*, 12668−12673.
(53) Khimji, I.; Kelly, E. Y.; Helwa, Y.; Hoang, M.; Liu, J. Visual Optical Biosensors Based on DNA-Functionalized Polyacrylamide Hydrogels. *Methods* **2013**, *64*, 292−298.
(54) Lee, B.-H.; Li, B.; Guelcher, S. A. Gel Microstructure Regulates Proliferation and Differentiation of MC3T3-E1 Cells Encapsulated in Alginate Beads. *Acta Biomater.* **2012**, *8*, 1693−1702.
(55) Lin, C.; Metters, A. Hydrogels in Controlled Release Formulations: Network Design and Mathematical Modelling. *Adv. Drug Delivery Rev.* **2006**, *58*, 1379−1408.
(56) Nguyen, Q. T.; Hwang, Y.; Chen, A. C.; Varghese, S.; Sah, R. L. Cartilage-Like Mechanical Properties of Poly (Ethylene Glycol)-Diacrylate Hydrogels. *Biomaterials* **2012**, *33*, 6682−6690.
(57) Cavallo, A.; Madaghiele, M.; Masullo, U.; Lionetto, M. G.; Sannino, A. Photo-Crosslinked Poly (Ethylene Glycol) Diacrylate (PEGDA) Hydrogels From Low Molecular Weight Prepolymer: Swelling and Permeation Studies. *J. Appl. Polym. Sci.* **2017**, *134*, 44380.
(58) Browning, M.; Wilems, T.; Hahn, M.; Cosgriff-Hernandez, E. Compositional Control of Poly (Ethylene Glycol) Hydrogel Modulus Independent of Mesh Size. *J. Biomed. Mater. Res., Part A* **2011**, *98*, 268−273.
(59) Gong, X.; Renegar, N.; Levi, R.; Strano, M. S. Machine Learning for the Discovery of Molecular Recognition Based on Single-Walled Carbon Nanotube Corona-Phases. *npj Comput. Mater.* **2022**, *8*, 135.
(60) Brandl, F.; Kastner, F.; Gschwind, R. M.; Blunk, T.; Teßmar, J.; Göpferich, A. Hydrogel-Based Drug Delivery Systems: Comparison of Drug Diffusivity and Release Kinetics. *J. Controlled Release* **2010**, *142*, 221−228.
(61) Esposito, G.; Giglio, E.; Pavel, N.; Zanobi, A. Size and Shape of Sodium Deoxycholate Micellar Aggregates. *J. Phys. Chem.* **1987**, *91*, 356−362.
(62) Bhattacharjee, J.; Verma, G.; Aswal, V.; Date, A. A.; Nagarsenker, M. S.; Hassan, P. Tween 80− Sodium Deoxycholate

Mixed Micelles: Structural Characterization and Application in Doxorubicin Delivery. *J. Phys. Chem. B* **2010**, *114*, 16414−16421.
(63) Cruise, G. M.; Scharp, D. S.; Hubbell, J. A. Characterization of Permeability And Network Structure of Interfacially Photopolymerized Poly (Ethylene Glycol) Diacrylate Hydrogels. *Biomaterials* **1998**, *19*, 1287−1294.
(64) Mangiapia, G.; D'Errico, G.; Capuano, F.; Ortona, O.; Heenan, R. K.; Paduano, L.; Sartorio, R. On The Interpretation of Transport Properties Of Sodium Cholate and Sodium Deoxycholate in Binary and Ternary Aqueous Mixtures. *Phys. Chem. Chem. Phys.* **2011**, *13*, 15906−15917.
(65) Chabala, L. D.; Gurney, A. M.; Lester, H. A. Dose-Response of Acetylcholine Receptor Channels Opened by a Flash-Activated Agonist in Voltage-Clamped Rat Myoballs. *J. Physiol.* **1986**, *371*, 407−433.
(66) Briskin, D.; Wang, P. Y.; Bartel, D. P. The Biochemical Basis for the Cooperative Action of Micrornas. *Proc. Natl. Acad. Sci. U.S.A.* **2020**, *117*, 17764−17774.
(67) Xhyliu, F.; Ao, G. Surface Coating- and Light-Controlled Oxygen Doping of Carbon Nanotubes. *J. Phys. Chem. C* **2021**, *125*, 9236−9243.
(68) Sims, C. M.; Fagan, J. A. Surfactant Chemistry and Polymer Choice Affect Single-Wall Carbon Nanotube Extraction Conditions in Aqueous Two-Polymer Phase Extraction. *Carbon* **2022**, *191*, 215−226.
(69) Fagan, J. A.; Becker, M. L.; Chun, J.; Nie, P.; Bauer, B. J.; Simpson, J. R.; Hight-Walker, A.; Hobbie, E. K. Centrifugal Length Separation of Carbon Nanotubes. *Langmuir* **2008**, *24*, 13880−13889.
(70) Roxbury, D.; Jena, P. V.; Shamay, Y.; Horoszko, C. P.; Heller, D. A. Cell Membrane Proteins Modulate the Carbon Nanotube Optical Bandgap via Surface Charge Accumulation. *ACS Nano* **2016**, *10*, 499−506.

https://doi.org/10.1021/acsami.2c16596
ACS Appl. Mater. Interfaces 2023, 15, 1772−1783